Flexible supercapacitors with high areal capacitance based on hierarchical carbon tubular nanostructures

CrossMark

Haitao Zhang [a], [**], Hai Su [a], Lei Zhang [a], Binbin Zhang [a], Fengjun Chun [a], Xiang Chu [a], Weidong He [b], Weiqing Yang [a], [*]

[a] *Key Laboratory of Advanced Technologies of Materials (Ministry of Education), School of Materials Science and Engineering, Southwest Jiaotong University, Chengdu 610031, China*
[b] *School of Energy Science and Engineering, University of Electronic Science and Technology, Chengdu, Sichuan 611731, China*

HIGHLIGHTS

- *h*CTNs are synthesized through direct conversion of carbon dioxide.
- Environmentally-friendly and simply preparing method.
- *h*CTNs can be effectively constructed on various substrates.
- *h*CTN electrodes show the maximum areal capacitance of ~320 mF cm^{-2}.
- *h*CTNs based flexible supercapacitors possess superior electrochemical properties.

GRAPHICAL ABSTRACT
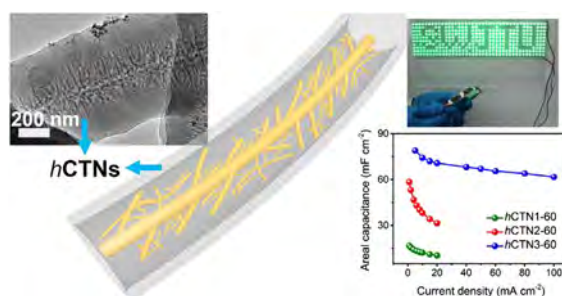
ABSTRACT

Hierarchical structure design can greatly enhance the unique properties of primary material(s) but suffers from complicated preparation process and difficult self-assembly of materials with different dimensionalities. Here we report on the growth of single carbon tubular nanostructures with hierarchical structure (*h*CTNs) through a simple method based on direct conversion of carbon dioxide. Resorting to in-situ transformation and self-assembly of carbon micro/nano-structures, the obtained *h*CTNs are blood-like multichannel hierarchy composed of one large channel across the *h*CTNs and plenty of small branches connected to each other. Due to the unique pore structure and high surface area, these *h*CTN-based flexible supercapacitors possess the highest areal capacitance of ~320 mF cm^{-2}, as well as good rate-capability and excellent cycling stability (95% retention after 2500 cycles). It was established that this method can control the morphology, size, and density of *h*CTNs and effectively construct *h*CTNs well anchored to the various substrates. Our work unambiguously demonstrated the potential of *h*CTNs for large flexible supercapacitors and integrated energy management electronics.

© 2016 Elsevier B.V. All rights reserved.

1. Introduction

The recent explosive development of flexible, portable, and wearable electronic devices has being inspired rapid development of their counterpart energy storage systems for providing efficient energy management [1,2]. Supercapacitors, also known as

---

* Corresponding author.
** Corresponding author.
E-mail addresses: haitaozhang@swjtu.edu.cn (H. Zhang), wqyang@swjtu.edu.cn (W. Yang).

electrochemical capacitors, have recently garnered intense interest as one kind of emerging flexible energy storage technologies [3–6]. Depending on different storage principles, supercapacitors can be divided into electrical double layer capacitors (EDLCs) represented by Helmholtz interface capacitor, and psuedocapacitors based on Faradaic reaction [7,8]. EDLCs based on electrostatic charge storage mechanism have high power density (>10 kW kg^{-1}) and an outstanding cycling stability. Consequently, supercapacitors complement or can even sometimes replace batteries in applications from microelectronics to transportation and the electrical grid, in which high-power delivery or uptake and super long cycle life are required [9,10].

Since EDLCs store the energy at the electrolyte/carbon interface by charging EDL capacitance, they suffer from low specific capacitance and low energy density (5–10 Wh kg^{-1}). These properties are largely determined by ion-accessible surface area, electrical conductivity, and pore structure of carbon materials [11–13]. Usually, through micro/nano-structural design to avoid the aggregation, provide efficient electron and ion transport pathways, and adjust the pore structure of carbon materials, superior capacitive performance and high energy density can be anticipated. And it is critical to further improve the properties of supercapacitors to achieve high specific capacitance and energy density for practical application.

Hierarchical structure design can greatly enhance unique properties of primary material(s) and has recently attracted great attention for fundamental investigations and potential applications in diverse technologies [14–20]. Inspired by the hierarchical structure in plants, carbon materials with hierarchical structure have been created through partial $\pi{-}\pi$ stacking interactions to form a 3D macrostructure with interconnected pores, which possesses a wide pore size distribution (PSD) *via* self-assembly of multi-dimension carbon materials [21–23]. The unique hierarchical structures feature high ion-accessible surface area, and superior carbon−electrolyte interface for efficient adsorption of ions from the electrolyte. They can ideally be used as supercapacitor electrodes with excellent specific capacitance, rate capability, and cycling stability. For example, a hierarchically structured carbon microfiber made of an interconnected network of carbon nanotubes and graphene with PVA/H$_3$PO$_4$ electrolyte exhibit a specific volumetric capacitance of 300 F cm^{-3} and a volumetric energy density of 6.3 mWh m^{-3} [24].

Although hierarchical carbon materials show great potential in supercapacitor electrode materials, they commonly suffer from the disadvantages of complicate preparation methods, consisting of composite materials, and high ratio of macropores [25–28]. Recently, many investigations have focused on the use of wet processing routes such as colloidal solutions or suspensions of particles for the electrode preparation [29,30]. These methods also have the drawbacks of low mass production and therefore it is difficult to develop flexible supercapacitors integrated with printable electronics.

In this work, hierarchical carbon tubular nanostructures (*h*CTNs) with 3D framework, linear, spring-like structure are created through direct conversion of carbon dioxide and shaped on multiple flexible substrates. The *h*CTNs are blood-vessel-like multichannel hiberarchy structure with carbon micro/nano-structures and possess good mechanical flexibility. A "main artery" runs through the whole *h*CTNs and a large number of "capillary vessels" spread over carbon micro/nano-structures with abundant micro to meso-pores. Particularly, these *h*CTNs with unique structure are suitable and effective electrode/electrolyte materials, and preferable structural designs to develop flexible power sources with better electrochemical performance for integration into flexible electronics. As expected, *h*CTN-based solid-state flexible supercapacitors exhibit high areal capacitance (321 mF cm^{-2} at 5 mV s^{-1} with PVA/H$_3$PO$_4$ electrolyte and 316 mF cm^{-2} at 5 mA cm^{-2} with PVA/KOH electrolyte) and excellent cycling stability (95% retention after 2500 cycles). In addition, our patterned *h*CTN supercapacitors with excellent performance could be integrated in serial or parallel connections to expand the output voltage or total capacitance to operate various active devices in need of variable operation voltage and current. The superior performance of these *h*CTNs evidently demonstrated the promise for applications in energy storage and then expansive energy management electronics.

2. Experimental

2.1. Preparation of hCTNs

The *h*CTNs were synthesized by a simple method of Mg reaction with CO$_2$ gas. To fabricate different substrate supporting *h*CTNs, Mg powders with a purity of 99.5% are spread on substrate like stainless steel meshes (500 meshes), wires, springs, and silicon wafers. In a typical process, 4.0 g Mg powders were put into a high purity corundum boat with a size of $100 \times 25 \times 20$ mm. Then the corundum boat was put into a tube furnace (GSL-1700X, Hefei Kejing Materials Tech. CO., Ltd., China) with a multichannel flow controller (GMF-2Z, AnHui BEQ Equipment Tech. CO., Ltd. China). And then Mg powders were heated to the aimed reaction temperature under the protection of Ar gas with flow rate of 20–200 sccm. Once the initial reaction temperature was achieved, the CO$_2$ gas with an equivalent volume of Ar was turned on. Through adjusting the position of the substrates and the reaction time, the morphology, size and density of *h*CTNs could be tailored. To emphasize the importance of some synthetic parameters, we named the samples as *h*CTNs*X-Y*, where *X* represents different substrate positions and *Y* represents different reaction time. The detailed information of substrate positions was illustrated in Supporting Fig. S1 and all the sample parameters were summarized in Table 1. After the reaction, the samples were treated by 1 M HCl aqueous solution for eliminating the impurities including Mg and

Table 1
The sample names and their concrete preparing parameters.

Sample names	Substrates	Position[a]	Time (min)
*h*CTN1-5	stainless steel mesh	left	5
*h*CTN2-5	stainless steel mesh	middle	5
*h*CTN3-5	stainless steel mesh	right	5
*h*CTN1-30	stainless steel mesh	left	30
*h*CTN2-30	stainless steel mesh	middle	30
*h*CTN3-30	stainless steel mesh	right	30
*h*CTN1-60	stainless steel mesh	left	60
*h*CTN2-60	stainless steel mesh	middle	60
*h*CTN3-60	stainless steel mesh	right	60
*h*CTN1-90	stainless steel mesh	left	90
*h*CTN2-90	stainless steel mesh	middle	90
*h*CTN3-90	stainless steel mesh	right	90
*h*CTN1-120	stainless steel mesh	left	120
*h*CTN2-120	stainless steel mesh	middle	120
*h*CTN3-120	stainless steel mesh	right	120
*h*CTN2-30S	stainless steel spring	middle	30
*h*CTN2-60Si	silicon wafer	middle	60
*h*CTN30[b]	/	/	30
*h*CTN60	/	/	60
*h*CTN90	/	/	90
*h*CTN120	/	/	120

Note.
[a] The substrate positions are shown in Fig. S1, where the positions are defined as left, middle, and right along the direction of the airflow from the left to right.
[b] The *h*CTN30 was powder of carbon tubular nanostructures without using the substrates, as well as the *h*CTN60, *h*CTN90 and *h*CTN120.

MgO particles. Finally, the samples were washed by abundant deionized water and alcohol, and then naturally dried.

2.2. The determination of areal mass loading of the samples

Since the substrate like stainless steel mesh is not completely stable at high temperature especially under Mg atmosphere that possess strong reducibility, the loading mass of *h*CTN samples can not simply determined by subtracting the mass of the substrate. After *h*CTNs were purified and dried, the mass of *h*CTNs and the substrate (M_1) were weighed. Then the samples were undergone robust ultrasonic processing for removing the *h*CTNs and further washed and dried prior to determining the mass of the substrate (M_2). Finally, the loading mass of the *h*CTN samples was obtained by M_1-M_2 and the areal loading mass of *h*CTN1-60, *h*CTN2-60, and *h*CTN3-60 is about 0.41 ± 0.06, 1.12 ± 0.10, and 1.27 ± 0.05 mg cm^{-2}, respectively. All the average values were deduced from the three batches and three samples by an electric balance with an accuracy of 0.01 mg (MS105DU, Mettler-Toledo, Switzerland).

2.3. Materials characterization

Scanning electron microscopy (SEM) images were recorded using a FEI QUANTA FEG 250 SEM in the high-vacuum mode with an accelerating voltage of 20 kV. Transmission electron microscopy (TEM) and high-resolution TEM (HRTEM) characterizations were taken using a JEOL JEM-2100F instrument. X-ray diffraction (XRD) of the samples was carried out with PNAalytical X'Pert Powder diffractometer with Cu Kα radiation between 10° and 70°. Raman spectra were measured using a Renishaw inVia Raman Microscope employing a 532 nm laser beam. Brunaue-Emmertt-Teller (BET) surface areas and density functional theory (DFT) pore size distribution measurements of *h*CTN powders were performed with Micromeritics ASAP 2020 surface area and pore size analyzer using nitrogen gas adsorption-desorption isotherm at -196 °C.

2.4. Synthesis of gel electrolytes

In order to synthesize PVA–H$_3$PO$_4$ gel electrolyte, 10 g PVA (1788 type), 100 mL deionized water, and 10 g of H$_3$PO$_4$ were mixed in a beaker at 85 °C until clear. For PVA–KOH gel electrolyte, 5 g PVA (1799 type) and 50 mL deionized water were mixed in a beaker at 85 °C until clear. And then 5 g KOH dissolved into 50 mL was mixed with the above solution at room temperature. Finally, the PVA–KOH clear solution with good mobility was prepared.

2.5. Fabrication of quasi-solid-state hCTN flexible supercapacitors

Two stainless steel meshes/*h*CTN electrodes were coated with PVA–H$_3$PO$_4$ or PVA–KOH gel electrolyte and placed in parallel to produce a symmetric sandwich-like supercapacitor. To assemble serial devices, the current collectors (e.g. stainless steel meshes) of two supercapacitors were connected head-to-tail by copper foil with polymer glue on one side. To encapsulate the *h*CTN supercapacitors, polydimethylsiloxane and silicone elastomer curing agent (PDMS, Dow Corning Corporation Midland, Michigan, USA) with a mass ratio of 10:1 were mixed and stirred witha glass rod. Then the bubbles were eliminated and a clear solution formed with good fluidity prior to use. Afterwards, the quasi-solid state *h*CTN electrodes were encapsulated by PDMS.

2.6. Electrochemical characterization

Cyclic voltammetry (CV) curves measured at the different scan rates ranging from 5 to 5000 mV s^{-1}, galvanostatic charge-discharge (GCD) process, electrochemical impedance spectroscopy (EIS) recorded in the frequency ranging from 100 kHz to 10 mHz with a 5 mV ac amplitude was carried out by a electrochemical workstation (CHI660E).

3. Results and discussion

Hierarchical carbon tubular nanostructures (*h*CTNs) are simply prepared by directly conversion of carbon dioxide using Mg metal as a reduction agent (Fig. 1a). The superstructures are blood-like multichannel hiberarchy structured by a "main artery" across the whole *h*CTNs and a large number of "capillary vessels" spread over carbon micro/nano-structures with abundant micro to meso-pores as represented by Fig. 1a. The growth mechanism of *h*CTN samples is related to metal liquid drop assisted growth along the axis of the nanotube which is driven by surface tension or capillary force, similar to water movement in the capillary tube [12]. Intriguingly, *h*CTNs can grow on different substrates including stainless steel (SS) wires, meshes, and springs as well as silicon substrates as shown in Fig. 1b. A SEM image of *h*CTNs uniformly grown on a SS mesh is shown in Fig. 1c. And *h*CTNs grown on other substrates like SS springs and silicon wafers are also shown (Supporting Figs. S2 and S3). Fig. 1d gives a single *h*CTNs with rough surface and a diameter of approximately 600 nm, which is quite larger than single and multi-walled carbon nanotubes [31–33].

The direct growth of hierarchical nanocarbons on various substrates provides some major advantages. First, chemical conversion through electron transfer reaction at solid-gas interface to synthesize hierarchical nanocarbons in a single step avoids multidimensional structural design and complex preparation process. Second, in comparison with preparing carbon nanotubes or graphene [34–37], the growth is not spatially restricted by the presence of a catalyst (as in the case of catalyst-deposited metal substrates), thus providing a simple way to fabricate hierarchical nanocarbons on various substrates. Third, the ability to grow hierarchical nanocarbons on a substrate of any shape or size provides tremendous flexibility for developing application where the morphology of the conductive substrates is critical.

Moreover, the morphology, size, and density of *h*CTNs can be tailored by adjusting the preparation parameters. Fig. 1e–g displays the SEM images of *h*CTN samples prepared at different substrate positions as above mentioned. It is clear that the samples obtained at different substrate positions possess similar tubular structure. However, adjusting the substrate positions is proved to be a key factor to affect the morphology and density of *h*CTNs. Far away from the gas flow direction, *h*CTN3-60 sample as shown in Fig. 1g has much a higher density than *h*CTN1-60 and *h*CTN2-60 as shown in Fig. 1e and f, respectively. The thickness of *h*CTN1-60, *h*CTN2-60 and *h*CTN3-60 are 16 ± 5 μm, 70 ± 8 μm, and 81 ± 7 μm, respectively excluding the thickness of the substrate. It is noted that hierarchical nanocarbon tubes grown at the interspace of SS materials are much longer than those on the surface in the horizontal dimension, indicating self-limited growth in a restrained space. On the other hand, the morphology and density of *h*CTN samples can be adjusted by varying the reaction time. Fig. 1h–k shows SEM images of *h*CTNs prepared at 5, 30, 60, and 90 min. With increasing reaction time, the tubular structure is maintained, and the *h*CTN networked architectures become much more compacted. In addition, low-resolution SEM images of the whole SS meshes supporting *h*CTN samples prepared at longer reaction time (such as *h*CTN2-60) unambiguously demonstrates that *h*CTNs fully cover the substrates, while it is not the case for shorter reaction time (e.g. *h*CTN2-30) as shown in Supporting Fig. S4.

Fig. 2 shows TEM and HRTEM images of *h*CTN samples obtained after directly conversion of CO$_2$ at 800 °C. Hierarchical tubular
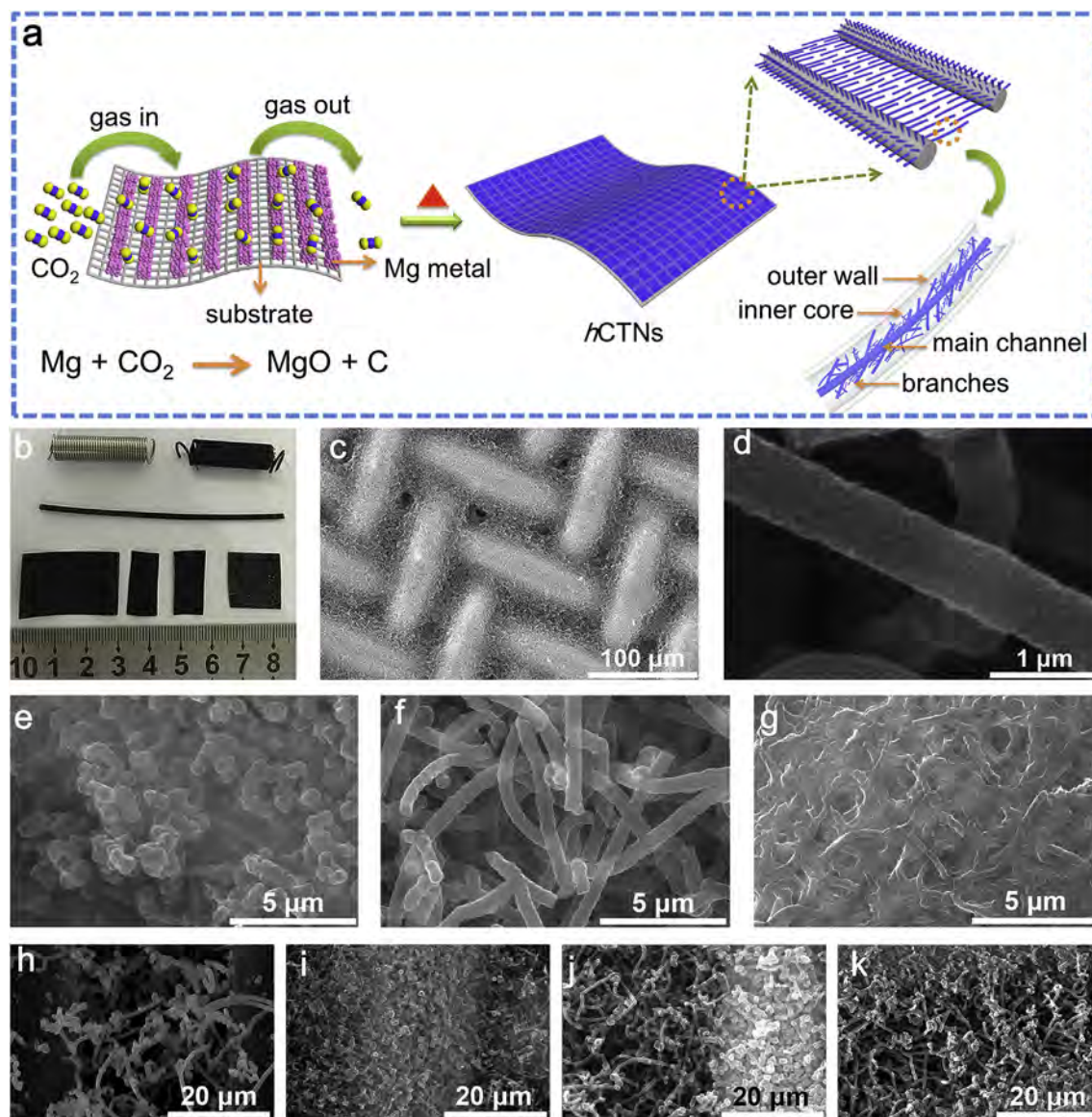
Fig. 1. Hierarchical carbon tubular nanostructures (*h*CTNs) grown on different geometries and different materials of substrates. (a) A schematic presentation of conversion of carbon dioxide into hierarchical carbon tubular nanostructures supported by the substrates. (b) A photograph of differently shaped and sized substrates used for *h*CTNs growth. The top-left and top-right are the as-received stainless steel spring and a similar substrate with *h*CTNs grown on it. A stainless steel wire and sheets are also shown. The bottom-right is the silicon substrate with *h*CTNs grown on it. (c) SEM images of *h*CTNs grown on a stainless steel mesh, showing that *h*CTNs can be uniformly covered on the whole mesh. (d) A high-resolution SEM image presenting tubular structure and rough surface of *h*CTNs. (e–g) The morphologies of *h*CTN networks can be tailored by varying the flow gases. (h–k) The density of *h*CTN networks on the stainless steel mesh can also be controlled by adjusting the reaction time.

carbons including *h*CTN1-60, *h*CTN2-60, and *h*CTN3-60 shown in Fig. 2a–c are clearly exhibited by TEM characterizations. The hierarchical structure is composed of one main tube channel across the *h*CTNs, around with a variety of hierarchies connected with each other as illustrated in Fig. 2d and e. Although all the samples are tubular like carbons, the *h*CTN2-60 and *h*CTN3-60 samples have larger tube diameter in axial direction than *h*CTN1-60. Thus, the substrate positions have important effect on the size, tube structure, and pore structure of *h*CTN samples. Another striking result is that the outer shell of *h*CTNs shows some degree of crystallinity (see Fig. 2h) while amorphous structure with rich of micro-to meso-pores for the inner cores (see Fig. 2i). The HRTEM images of *h*CTN1-60 and *h*CTN2-60 have similar wall structure (Supporting Fig. S5). By the way, the inner cores show amorphous structure for the *h*CTN3-60 as shown in Fig. 2h, similar for *h*CTN1-60 and *h*CTN2-60 (Supporting Fig. S6), which is also coincident with the XRD

results (Supporting Fig. S7). And *h*CTNs present high ratio of structural defects demonstrated by a strong broad *D*-band peak of Raman spectra for each sample (Supporting Fig. S8a and S8b). The ratio of I_D/I_G determined by the multi-peak fit (four Gauss function for *D*, *D'*, *D''*, and *G* bands) are 1.16 ± 0.07, 1.31 ± 0.07, 1.43 ± 0.08, 1.53 ± 0.04, and 1.97 ± 0.07 with increasing the reaction time from 5 to 90 min (Supporting Fig. S8c and S8d). It is interesting that novel carbon hierarchical structure is obtained by a simple preparing method based on solid-gas reaction. We proved that *h*CTN samples possess well micro-to meso-pore distribution detected by density functional theory calculation (Fig. 2i). The BET surface areas of *h*CTN powders show an increase from 460 to 831 m^2 g^{-1} with increasing the reaction time from 30 to 90 min, but decreases to 709 m^2 g^{-1} with further increasing the reaction time to 120 min (Supporting Fig. S9a). Similarly, pore size distribution calculated by BJH method proved that *h*CTNs possess hierarchical pore structure with micro-
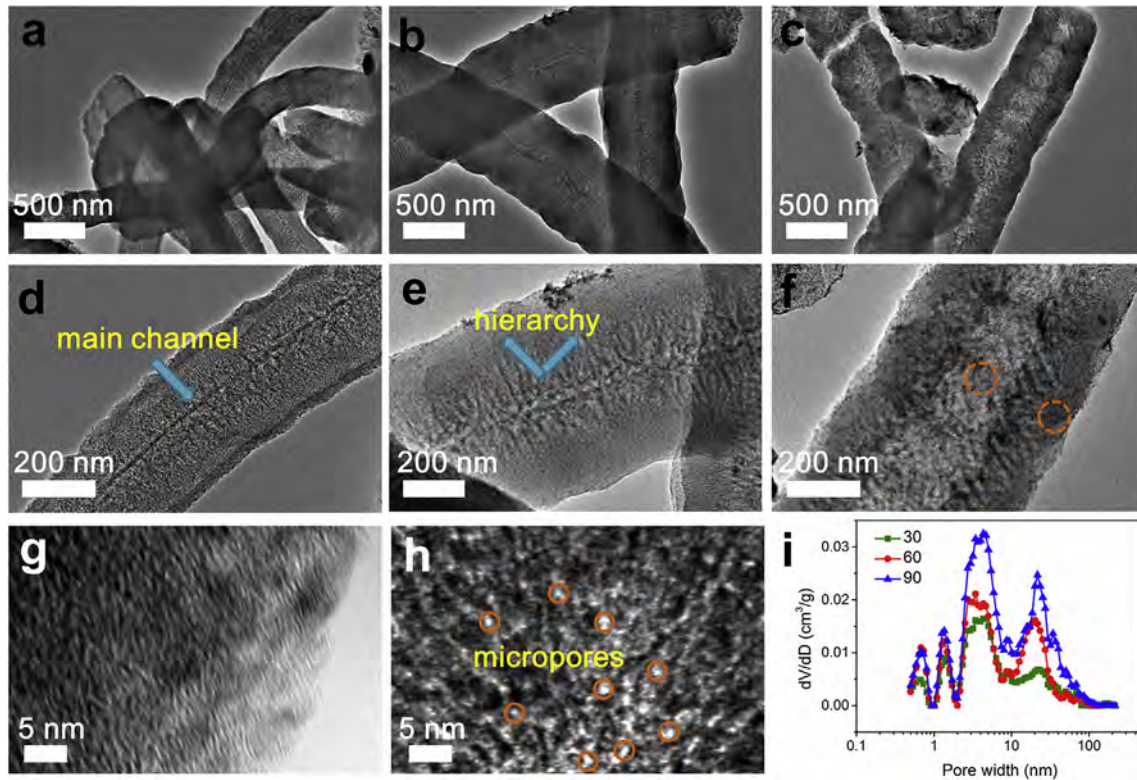
Fig. 2. TEM images of (a) *h*CTN1-60, (b) *h*CTN2-60, (c) *h*CTN3-60, and (d–f) the correspondingly enlarged images of individual *h*CTN shown in (a–c). (g, h) HRTEM images of the outer wall and inner core structure of *h*CTN3-60 sample, (i) Pore size distribution calculated by density functional theory.

to meso-pores (Supporting Fig. S9b). In addition, the decrease BET surface area of *h*CTN120 can be attributed from the structural damage (Supporting Fig. S10) with further prolonging the reaction time.

Since *h*CTNs have unique hierarchical structure and relatively high surface area, which is critical to the capacitive energy storage. Substrates like SS meshes and springs supported *h*CTNs have good mechanical flexibility, and we assemble two-electrode configuration in gel electrolyte to better reflect the capacitive energy storage process. Fig. 3a illustrates the schematic representation of quasi-solid-state flexible supercapacitors with PVA/H₃PO₄ gel electrolyte functioned as not only a conducting medium, but also as a separator to prevent short circuits. Some partial of the substrate as the current collector is intentionally exposed from the gel electrolyte and the PDMS package. With PVA/H₃PO₄ gel electrolyte, *h*CTN supercapacitors can be reversibly charged and discharged with a voltage window of 1.0–1.2 V (Supporting Fig. S11). The assembled devices can be randomly bended, folded, and even twisted (see Fig. 3b). Under mechanical bending, folding, and twisting loads, the *h*CTN2-60 based flexible supercapacitors at a scan rate of 100 mV s⁻¹ shows 100%, 97.4%, and 96.3% capacitance retentions as illustrated in Fig. 3c. All the CV curves exhibit a rectangular shape at scan rates from 10 to 1000 mV s⁻¹ (see Fig. 3c and Supporting Fig. S12), indicating good capacitive behavior and high rate-capability for solid-state flexible supercapacitors.

Fig. 3d shows that *h*CTN3-60 flexible supercapacitors have the highest specific areal capacitance, ~80 mF cm⁻² (321 mF cm⁻² for a single *h*CTN3-60 electrode) at 5 mV s⁻¹, which is much higher than previously reported nanocarbon-based capacitive energy storage [38–43]. The specific areal capacitance decreases with increasing scan rates, that is, 66, 44, 32, 26, 22, and 19 mF cm⁻² at 10, 20, 40, 60, 80, and 100 mV s⁻¹. Although, *h*CTN1-60 and *h*CTN2-60 show

low areal capacitance, that is 78 and 15 mF cm⁻² at a scan rate of 5 mV s⁻¹, they show high capacitance retentions of 50.7% and 57.7% when the scan rate increases to 1000 mV s⁻¹ (7.6 and 45 mF cm⁻² for *h*CTN1-60 and *h*CTN2-60 flexible supercapacitors). Moreover, the capacitance maintains 95% after cycling for 2500 cycles at a scan rate of 1000 mV s⁻¹ for *h*CTN1-60 based supercapacitors (Fig. 3e). Their remarkable electrochemical performance of the *h*CTNs may be attributable to the excellent electrical and mechanical properties of the tubular nanocarbon networks overcoming obstacles to application in interconnect and contact technologies for electrical transport and physical support. More importantly, the diffusion length is short for electrolyte ions in unique hierarchical pore structure, which leads to higher specific areal capacitances and superior rate capabilities.

In addition to using individual device, our patterned *h*CTN supercapacitors with excellent performance could be integrated in serial or parallel connections to expand the output voltage or the total capacitance. Fig. 3f shows GCD curves of one, three and three *h*CTN supercapacitors assembled in parallel and in serial, respectively. The *h*CTN supercapacitors were charged and discharged at 5 mA cm⁻². The charge/discharge voltage windows of the device arrays in serial can be multiplied by the number of *h*CTN supercapacitors integrated to 3 V with similar discharge times. When operated at the same current density, the parallel device array shows 1.5 times higher in the discharge time than that of single *h*CTN supercapacitors. Theoretically, it should possess two times higher and the loss may be ascribed to the discrepancy thickness of the *h*CTN electrodes as above discussed. The inset of Fig. 3f shows a photograph of three *h*CTN supercapacitors connected in serial to turn on a pattern of nearly 400 light-emitting diodes (LEDs), which can be operated by an applied voltage of 3.0 V. The bottom, middle, and top insets are photographs of the flexible *h*CTN
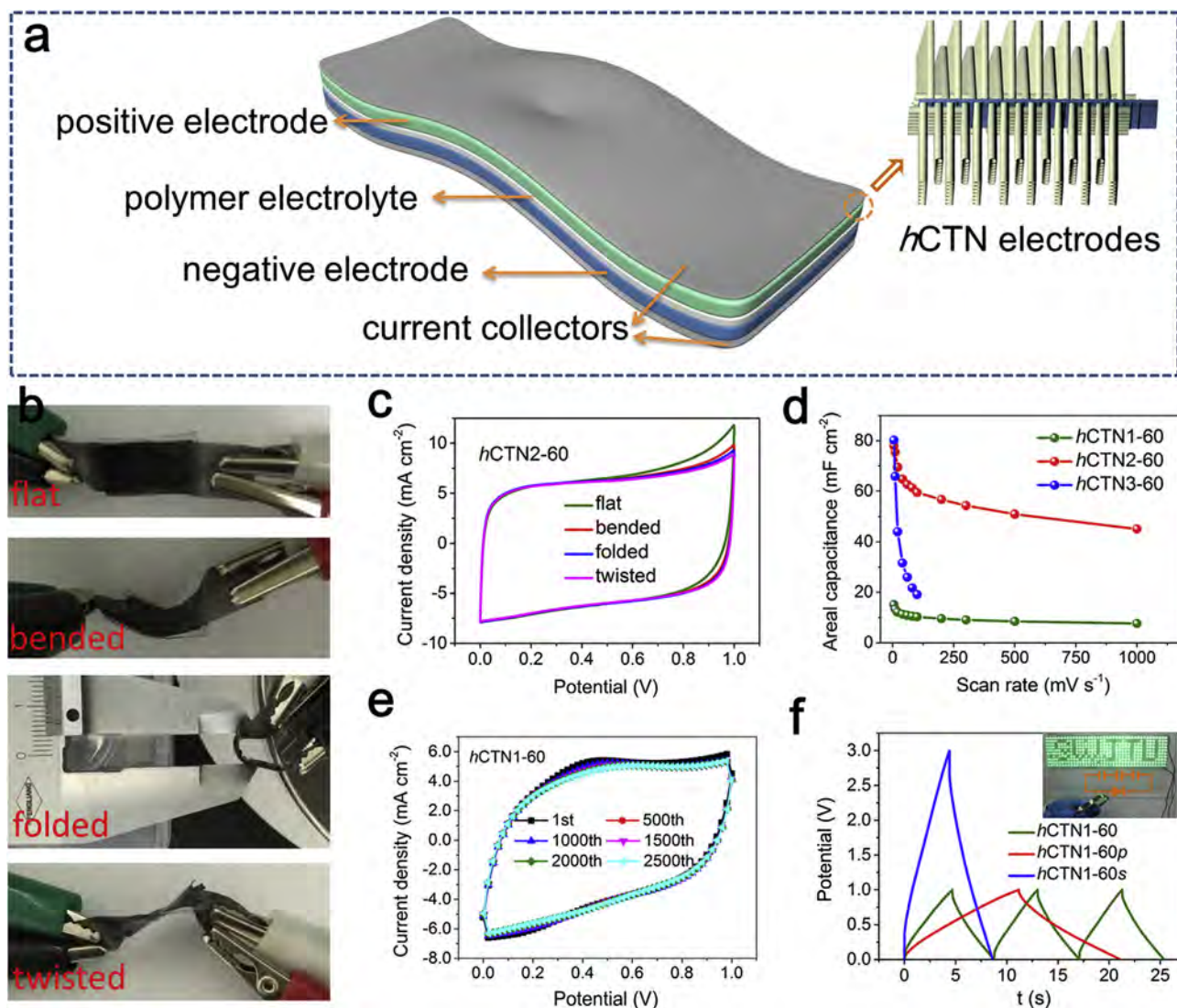
Fig. 3. The electrochemical properties of *h*CTN-based flexible supercapacitors with PVA/H₃PO₄ gel electrolyte. (a) Schematic illustration of quasi-solid state *h*CTN flexible super-capacitors. (b) Flexible supercapcaitors with *h*CTN electrodes can be mechanically bended, folded, and twisted. (c) CV curves of *h*CTN supercapacitors under different mechanical load, and (d) the areal capacitance at different scan rates of *h*CTN1-60, *h*CTN2-60, and *h*CTN3-60 flexible supercapacitors. (e) Cycling stability of *h*CTN1-60 flexible supercapacitors, the scan rate is 1000 mV s⁻¹. (f) Charge-discharge curves at a current density of 5 mA for three *h*CTN supercapacitors interconnected in serial (blue), parallel (red), for comparing, single *h*CTN supercapacitors are also shown (olive). The inset shows photograph of three serially connected flexible *h*CTN supercapacitors turning on a pattern of nearly 400 LEDs. The bottom, middle, and top insets are photographs of the flexible *h*CTN supercapacitors, circuit diagram of three serially connected *h*CTN supercapacitors with a resistor, and a pattern of LEDs, respectively. (For interpretation of the references to colour in this figure legend, the reader is referred to the web version of this article.)

supercapacitors, circuit diagram of three serially connected *h*CTN supercapacitors with a resistor, and a pattern of LEDs, respectively. These results clearly demonstrate that the mechanically stable *h*CTN supercapacitors, which can be integrated into a circuit to operate various active devices in need of variable operation voltage and current.

Similarly, *h*CTN supercapacitors with PVA + KOH gel electrolyte can be randomly bended, folded, and twisted. The current densities remain the constant under these mechanical loads, indicating 100% capacitance retention for all the flexible supercapacitors (Fig. 4a). The power capability of supercapacitors depends strongly on the internal resistances. In the meanwhile, the EIS is an effective method to evaluate the related parameters. In this regard, EIS shown in Fig. 4b was used to study the *h*CTN supercapacitors. It clearly shows that the *h*CTN based supercapacitors with PVA + KOH gel electrolyte exhibit a vertical line at the low frequency, indicating a good EDL capacitance. This result is further proved by a high

phase angle of 82.5–83.8° at a low frequency of 0.01 Hz (Fig. 3c). Moreover, all the *h*CTN based supercapaciotrs possess rapid electrochemical response as implied by low values of relaxation time constant $\tau_0 = 1/f_0 \approx 0.25$, 1.0, and 0.5 s for *h*CTN1-60, *h*CTN2-60, and *h*CTN3-60 flexible supercapacitors. Similar trends can be observed for the charge transfer and ion diffusion resistance from the radius of the semicircles and the Warburg region on the Nyquist plot. The equivalent distributed resistance (*EDR*) obtained from the *X*-intercept on the Nyquist plot are respectively 6.2, 4.5, and 1.8 Ω for *h*CTN1-60, *h*CTN2-60, and *h*CTN3-60 flexible supercapacitors, which are determined by using a method reported by R. Kötz et al. [44].

Fig. 4d shows the areal capacitance of the *h*CTN supercapacitor with PVA/KOH electrolytes at the current densities ranging from 1 to 100 mA cm⁻². The maximum areal capacitance in PVA/KOH electrolytes were calculated as 79.0 mF cm⁻² (316 mF cm⁻² for a single electrode) for *h*CTN3-60 sample at a current density of
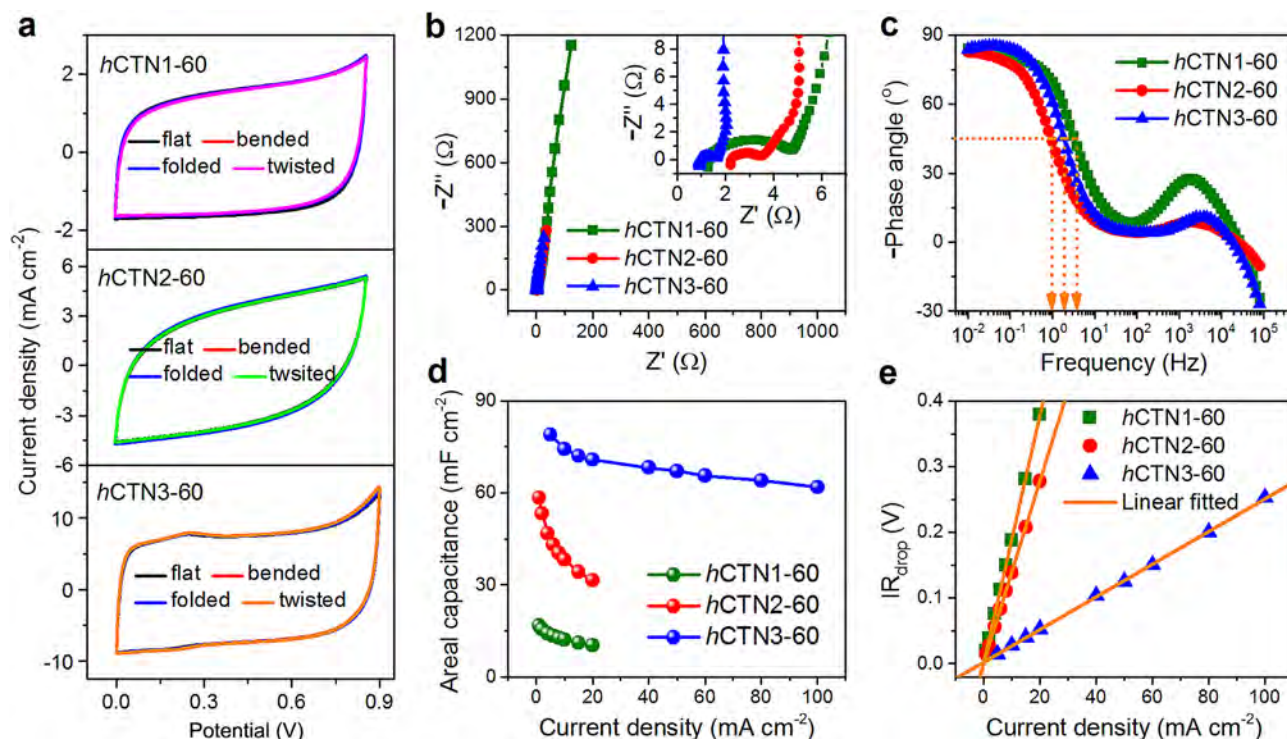
Fig. 4. The electrochemical properties of *h*CTN-based flexible supercapacitors with PVA/KOH gel electrolyte. (a) The CV curves at 100 mV s^{-1} under different mechanical loads. (b) EIS plots and (c) phase angle depends on the frequency. (d) The areal capacitance at different galvanostatic charge-discharge (GCD) current densities for *h*CTN1-60, *h*CTN2-60, and *h*CTN3-60 flexible supercapacitors. (e) The IR drop as a function of the different current densities calculated by the GCD curves.

5 mA cm^{-2}, which are 373% and 35% higher than that of *h*CTN1-60 and *h*CTN2-60 supercapacitors (16.7 and 58.4 mF cm^{-2} at a current density of 1 mA cm^{-2}). And the corresponding mass capacitance for *h*CTN1-60, *h*CTN2-60 and *h*CTN3-60 single electrode is 163 ± 25, 209 ± 20, and 249 ± 10 F g^{-1}, respectively. Based on the above discussion, the maximum areal capacitance for *h*CTN3-60 flexible supercapacitors with either PVA/H$_3$PO$_4$ or PVA/KOH electrolytes almost remains the same. Importantly, the areal capacitances of *h*CTN3-60 retain 70.8, 67.1, and 61.8 mF cm^{-2} at high current densities of 20, 50, and 100 mA cm^{-2}. The areal capacitance of *h*CTNs decreases slightly with the increase of charge/discharge rates, suggesting good rate capability of the *h*CTN based supercapacitor. The equivalent series resistance (*ESR*) and *EDR* of *h*CTN electrodes with PVA/KOH gel electrolyte are as low as 1.4, 2.3, 1.0 Ω, and 6.5, 5.0, 2.0 Ω, respectively for *h*CTN1-60, *h*CTN2-60 and *h*CTN3-60 supercapacitors and it induced IR drop shows an excellent linear relation on the dependence of the measured current densities (Fig. 4e). However, the IR drop induced by the internal resistance is a little bit large, which may be attributed that the structure inside the *h*CTN is more like that of amorphous carbon on one hand, on the other hand, the quasi-solid-state gel electrolyte show inferior electrical conductivity and ionic transfer. Here we also proved that *h*CTN samples have high areal capacitance and excellent rate-capability in 6 M KOH aqueous solution (Supporting Fig. S13).

4. Conclusion

In conclusion, we have demonstrated that hierarchical carbon tubular nanostructures with good flexibility and low contact resistance can be grown directly on various substrates using a simple method of Mg reaction with carbon dioxide. Chemical conversion of hierarchical nanostructures *via* electron transfer

reaction occurred on solid-gas interface can overcome the difficulties associated with controlling the morphology, size, and chemical composition in conventional syntheses. Flexible supercapacitors based on *h*CTNs exhibit high areal capacitance, excellent electrochemical stability and good rate-capability. The superior electrochemical performance is achieved by adopting multi-dimensional pore structure for its full utilization of the electrode materials. Herein reported the capability of designing hierarchical carbon tubular nanostructures on the versatile substrates is that overcoming obstacles to applications in interconnect and contact technologies, supercapacitors, and will also open up new possibilities for practical applications.

Appendix A. Supplementary data

Supplementary data related to this article can be found at http://dx.doi.org/10.1016/j.jpowsour.2016.09.064.

References

[1] L. Li, Z. Wu, S. Yuan, X.-B. Zhang, Energy Environ. Sci. 7 (2014) 2101.
[2] Y.M. He, W.J. Chen, C.T. Gao, J.Y. Zhou, X.D. Li, E.Q. Xie, Nanoscale 5 (2013) 8799−8820.
[3] Y.Z. Zhang, Y. Wang, T. Cheng, W.Y. Lai, H. Pang, W. Huang, Chem. Soc. Rev. 44

(2015) 5181–5199.

[4] H.T. Zhang, K. Wang, X. Zhang, H. Lin, X.Z. Sun, C. Li, Y.W. Ma, J. Mater. Chem. A 3 (2015) 11277–11286.

[5] J. Vatamanu, D. Bedrov, J. Phys. Chem. Lett. 6 (2015) 3594–3609.

[6] S. Wang, L. Ma, M. Gan, S. Fu, W. Dai, T. Zhou, X. Sun, H. Wang, H. Wang, J. Power Sources 299 (2015) 347–355.

[7] B.E. Conway, J. Electrochem. Soc. 138 (1991) 1539–1548.

[8] G. Xu, J. Yuan, X. Tao, B. Ding, H. Dou, X. Yan, Y. Xiao, X. Zhang, Nano Res. 8 (2015) 3066–3074.

[9] P. Simon, Y. Gogotsi, Nat. Mater. 7 (2008) 845–854.

[10] P. Huang, C. Lethien, S. Pinaud, K. Brousse, R. Laloo, V. Turq, M. Respaud, A. Demortière, B. Daffos, P.L. Taberna, B. Chaudret, Y. Gogotsi, P. Simon, Science 351 (2016) 691–695.

[11] L. Zhang, X. Yang, F. Zhang, G.K. Long, T.F. Zhang, K. Leng, Y.W. Zhang, Y. Huang, Y.F. Ma, M.T. Zhang, Y.S. Chen, J. Am. Chem. Soc. 135 (2013) 5921–5929.

[12] H. Zhang, X. Zhang, Y. Ma, Electrochim. Acta 184 (2015) 347–355.

[13] H.T. Zhang, X. Zhang, X.Z. Sun, Y.W. Ma, Sci. Rep. 3 (2013) 3534.

[14] Z. Xu, X. Zhuang, C. Yang, J. Cao, Z. Yao, Y. Tang, J. Jiang, D. Wu, X. Feng, Adv. Mater. 28 (2016) 1981–1987.

[15] K.W. Tan, B. Jung, J.G. Werner, E.R. Rhoades, M.O. Thompson, U. Wiesner, Science 349 (2015) 54–58.

[16] J.K. Sun, Q. Xu, Chem. Commun. 50 (2014) 13502–13505.

[17] T.Y. Yang, R.F. Zhou, D.W. Wang, S.P. Jiang, Y. Yamauchi, S.Z. Qiao, M.J. Monteiro, J. Liu, Chem. Commun. 51 (2015) 2518–2521.

[18] J. Kuang, Z.H. Dai, L.Q. Liu, Z. Yang, M. Jin, Z. Zhang, Nanoscale 7 (2015) 9252–9260.

[19] G.H. An, J.I. Sohn, H.J. Ahn, J. Mater. Chem. A 4 (2016) 2049–2054.

[20] L. Zhang, H. Zhang, L. Jin, B. Zhang, F. Liu, H. Su, F. Chun, Q. Li, J. Peng, W. Yang, RSC Adv. 6 (2016) 50209.

[21] H. Jiang, P.S. Lee, C. Li, Energy Environ. Sci. 6 (2013) 41–53.

[22] H. Zhang, L. Zhang, J. Chen, H. Su, F. Liu, W. Yang, J. Power Sources 315 (2016) 120–126.

[23] Z.S. Wu, Y. Sun, Y.Z. Tan, S.B. Yang, X.L. Feng, K. Mullen, J. Am. Chem. Soc. 134 (2012) 19532–19535.

[24] D.S. Yu, K. Goh, H. Wang, L. Wei, W.C. Jiang, Q. Zhang, L.M. Dai, Y. Chen, Nat.

[25] Y.-S. Hu, P. Adelhelm, B.M. Smarsly, S. Hore, M. Antonietti, J. Maier, Adv. Funct. Mater. 17 (2007) 1873–1878.

[26] D.W. Wang, F. Li, M. Liu, G.Q. Lu, H.M. Cheng, Angew. Chem. Int. Ed. 48 (2009), 1525–1525.

[27] J. Biener, M. Stadermann, M. Suss, M.A. Worsley, M.M. Biener, K.A. Rose, T.F. Baumann, Energy Environ. Sci. 4 (2011) 656–667.

[28] M.Q. Zhao, Q. Zhang, J.Q. Huang, F. Wei, Adv. Funct. Mater. 22 (2012) 675–694.

[29] S. Nardecchia, D. Carriazo, M.L. Ferrer, M.C. Gutierrez, F. del Monte, Chem. Soc. Rev. 42 (2013) 794–830.

[30] P. Strubel, S. Thieme, T. Biemelt, A. Helmer, M. Oschatz, J. Bruckner, H. Althues, S. Kaskel, Adv. Funct. Mater. 25 (2015) 287–297.

[31] U. Khalilov, A. Bogaerts, E.C. Neyts, Nat. Commun. 6 (2015) 10306.

[32] G. Ning, C. Xu, X. Zhu, R. Zhang, W. Qian, F. Wei, Z. Fan, J. Gao, Carbon 56 (2013) 38–44.

[33] M.F.L. De Volder, S.H. Tawfick, R.H. Baughman, A.J. Hart, Science 339 (2013) 535–539.

[34] D.N. Futaba, K. Hata, T. Yamada, T. Hiraoka, Y. Hayamizu, Y. Kakudate, O. Tanaike, H. Hatori, M. Yumura, S. Iijima, Nat. Mater. 5 (2006) 987–994.

[35] K.S. Kim, Y. Zhao, H. Jang, S.Y. Lee, J.M. Kim, K.S. Kim, J.H. Ahn, P. Kim, J.Y. Choi, B.H. Hong, Nature 457 (2009) 706–710.

[36] A.J. Strudwick, N.E. Weber, M.G. Schwab, M. Kettner, R.T. Weitz, J.R. Wunsch, K. Mullen, H. Sachdev, ACS Nano 9 (2015) 31–42.

[37] K.W. Kim, W. Song, M.W. Jung, M.-A. Kang, S.Y. Kwon, S. Myung, J. Lim, S.S. Lee, K.-S. An, Carbon 82 (2015) 96–102.

[38] M.F. El-Kady, V. Strong, S. Dubin, R.B. Kaner, Science 335 (2012) 1326–1330.

[39] G. Huang, C. Hou, Y. Shao, B. Zhu, B. Jia, H. Wang, Q. Zhang, Y. Li, Nano Energy 12 (2015) 26–32.

[40] Z. Xiong, C. Liao, W. Han, X. Wang, Adv. Mater. 27 (2015) 4469–4475.

[41] X. Li, X. Zang, Z. Li, X. Li, P. Li, P. Sun, X. Lee, R. Zhang, Z. Huang, K. Wang, D. Wu, F. Kang, H. Zhu, Adv. Funct. Mater. 23 (2013) 4862–4869.

[42] Q. Zheng, Z. Cai, Z. Ma, S. Gong, ACS Appl. Mater. Inter. 7 (2015) 3263–3271.

[43] J. Chen, K.X. Sheng, P.H. Luo, C. Li, G.Q. Shi, Adv. Mater. 24 (2012) 4569–4573.

[44] D. Weingarth, D. Cericola, F.C.F. Mornaghini, T. Hucke, R. Kötz, J. Power Sources 266 (2014) 475–480.